

1

2 **Main Manuscript for**

3 A redox switch allows binding of Fe(II) and Fe(III) ions in the
4 cyanobacterial iron binding protein FutA from *Prochlorococcus*

5 **Rachel Bolton^{a,b}, Moritz M. Machelett^{a,c}, Jack Stubbs^{a,b}, Danny Axford^b, Nicolas**
6 **Caramello^{d,e}, Lucrezia Catapano^{f,g}, Martin Malý^a, Matthew J. Rodrigues^{a,b,h}, Charlotte**
7 **Cordery^{a,b}, Graham J. Tizzardⁱ, Fraser MacMillan^j, Sylvain Engilberge^d, David von Stetten^k,**
8 **Takehiko Tosh^l, Hiroshi Sugimoto^l, Jonathan A.R. Worrall^m, Jeremy S. Webb^{a,b}, Mike**
9 **Zubkov^{c,n}, Simon Colesⁱ, Eric Mathieu^o, Roberto A. Steiner^{f,p}, Garib Murshudov^g, Tobias E.**
10 **Schrader^q, Allen M. Orville^{b,r}, Antoine Royant^{d,o}, Gwyndaf Evans^{b,s}, Michael A. Hough^{b,m,r},**
11 **Robin L. Owen^b, Ivo Tews^a**

12 ^a Biological Sciences, Institute for Life Sciences, University of Southampton, Southampton, SO17
13 1BJ, UK

14 ^b Diamond Light Source, Harwell Science and Innovation Campus, Didcot, Oxfordshire, OX11
15 0DE, UK

16 ^c National Oceanography Centre, Southampton SO14 3ZH, UK

17 ^d European Synchrotron Radiation Facility, 38043 Grenoble Cedex 9, France

18 ^e Hamburg Centre for Ultrafast Imaging, HARBOR, Universität Hamburg, Luruper Chaussee 149,
19 22761 Hamburg, Germany

20 ^f Randall Centre of Cell and Molecular Biophysics, King's College London, New Hunt's House,
21 Guy's Campus, London, SE1 1UL, UK

22 ^g MRC Laboratory of Molecular Biology, Francis Crick Avenue, Cambridge Biomedical Campus,
23 Cambridge, CB2 0QH, UK

24 ^h Laboratory of Biomolecular Research, Paul Scherrer Institute, 5232 Villigen, Switzerland

25 ⁱ School of Chemistry, University of Southampton, Southampton, SO17 1BJ, UK

26 ^j School of Chemistry, University of East Anglia, Norwich NR4 7TJ, UK

27 ^k European Molecular Biology Laboratory (EMBL), Hamburg Unit, Notkestraße 85, 22607
28 Hamburg, Germany

29 ^l Synchrotron Radiation Life Science Instrumentation Team, RIKEN SPring-8 Center, 1-1-1 Kouto,
30 Sayo, Hyogo 679-5148, Japan

31 ^m School of Life Sciences, University of Essex, Wivenhoe Park, Colchester CO4 3SQ, UK

32 ⁿ Scottish Association for Marine Science, Oban PA37 1QA, Scotland, UK

33 ^o Univ. Grenoble Alpes, CNRS, CEA, Institut de Biologie Structurale (IBS), 38044 Grenoble
34 Cedex 9, France

35 ^p Department of Biomedical Sciences, University of Padova, via Ugo Bassi 58/B, 35131 Padova,
36 Italy

37 ^q Forschungszentrum Jülich GmbH, Jülich Centre for Neutron Science (JCNS), Lichtenbergstraße
38 1, 85748 Garching, Germany

39 ^r Research Complex at Harwell, Harwell Science and Innovation Campus, Didcot, OX11 0FA,
40 United Kingdom

41 ^s Rosalind Franklin Institute, Harwell Science and Innovation Campus, Didcot, Oxfordshire, OX11
42 0QX, UK

43 *Corresponding author: Ivo Tews, Biological Sciences, Institute for Life Sciences, University of
44 Southampton, Southampton, SO17 1BJ, UK, m: ivo.tews@soton.ac.uk

45 **Email:** ivo.tews@soton.ac.uk

46 **Author Contributions:** Investigation: RB, MMM, JS, DA, NC, CC, GJT, FMM, SE, EM, TS, AR,
47 MH, RLO, IT; Formal Analysis: RB, JS, DA, NC, LC, MM, MJR, FMM, TS, AR, IT; Methodology:
48 DA, NC, LC, MJR, SE, DvS, TT, HS, JW, RAS, GM, TS, AR, MH, RLO, IT; Funding acquisition:
49 JSW, MZ, SC, AMO, GE, MH, IT; Writing – original draft: RB, MMM, IT, Writing – review &
50 editing: RB, DA, AMO, AR, MH, RLO, IT.

51 **Competing Interest Statement:** The authors do not declare competing interests.

52 **Classification:** Biological Sciences / Biophysics and Computational Biology.

53 **Keywords:** cyanobacteria, serial femtosecond crystallography, radiation damage, iron, ABC
54 transporter.

55 **This file includes:**

56 Main Text
57 Figures 1 to 4

58 **Abstract**

59 The marine cyanobacterium *Prochlorococcus* is a main contributor to global photosynthesis,
60 whilst being limited by iron availability. Cyanobacterial genomes typically encode two different
61 types of FutA iron binding proteins: periplasmic FutA2 ABC transporter subunits bind Fe(III), while
62 cytosolic FutA1 binds Fe(II). Owing to their small size and their economized genome
63 *Prochlorococcus* ecotypes typically possess a single *futA* gene. How the encoded FutA protein
64 might bind different Fe oxidation states was previously unknown. Here we use structural biology
65 techniques at room temperature to probe the dynamic behavior of FutA. Neutron diffraction
66 confirmed four negatively charged tyrosinates, that together with a neutral water molecule
67 coordinate iron in trigonal bipyramidal geometry. Positioning of the positively charged Arg103 side
68 chain in the second coordination shell yields an overall charge-neutral Fe(III) binding state in
69 structures determined by neutron diffraction and serial femtosecond crystallography.
70 Conventional rotation X-ray crystallography using a home source revealed X-ray induced
71 photoreduction of the iron center with observation of the Fe(II) binding state; here, an additional
72 positioning of the Arg203 side chain in the second coordination shell maintained an overall
73 charge neutral Fe(II) binding site. Dose series using serial synchrotron crystallography and an
74 XFEL X-ray pump-probe approach capture the transition between Fe(III) and Fe(II) states,
75 revealing how Arg203 operates as a switch to accommodate the different iron oxidation states.
76 This switching ability of the *Prochlorococcus* FutA protein may reflect ecological adaptation by
77 genome streamlining and loss of specialized FutA proteins.

78 **Significance Statement**

79 Oceanic primary production by marine cyanobacteria is a main contributor to carbon and nitrogen
80 fixation. *Prochlorococcus* is the most abundant photosynthetic organism on Earth, with an annual
81 carbon fixation comparable to the net global primary production from agriculture. Its remarkable
82 ecological success is based on the ability to thrive in low nutrient waters. To manage iron
83 limitation, *Prochlorococcus* possesses the FutA protein for iron uptake and homeostasis. We
84 reveal a molecular switch in the FutA protein that allows it to accommodate binding of iron in
85 either the Fe(III) or Fe(II) state using structural biology techniques at room temperature and
86 provide a plausible mechanism for iron binding promiscuity.

87 **Main Text**

88 **Introduction**

89 Iron is the fourth most abundant element in the Earth's crust (1). However, because of the poor
90 solubility, primary production in large oceanic and freshwater environments is limited by iron
91 uptake (2). In oxygenated aqueous environments, iron predominantly exists in Fe(III)
92 oxyhydroxides (3) with a solubility of 10^{-18} M (4) and consequently precipitates to severely limit
93 bioavailability (5). Marine phytoplankton require iron in the photosynthetic electron transport chain
94 (6) and in the nitrogenase enzyme (7, 8); thus, iron availability directly limits photosynthesis (9)
95 and nitrogen fixation (10).

96 Cyanobacteria of the *Prochlorococcus* genus are able to fix four gigatons of carbon per annum,
97 which is comparable to the net primary production of global agriculture (11). *Prochlorococcus*
98 bacteria dominate bacterial populations in tropical and subtropical oligotrophic ocean regions
99 (12). One of the factors for ecological success is the exceptional ability of this bacterium to thrive
100 in low nutrient waters (13). Adaptation includes reduction in size to 0.5 – 0.7 μ m, making
101 *Prochlorococcus* not only the most abundant but also the smallest photosynthetic organism on
102 Earth (14). Reduction in size maximizes the surface-area-to-volume ratio for metabolic efficiency,
103 to a tradeoff of genome reduction, and *Prochlorococcus* maintains the smallest genome (1.6-2.7
104 Mb) known for any free-living phototroph (15).

105 Typically, cyanobacteria harbor multiple iron uptake systems (16). In the common TonB transport
106 system, organic ligands (siderophores) are used to solubilize iron (17). The majority of the
107 *Prochlorococcus* species lack genes for siderophore biosynthesis (18, 19); instead, the bacterium
108 relies on the Fut ABC transporter for iron uptake (20). Here, specialized periplasmic proteins
109 sequester elemental iron (16); FutA2 is such a substrate binding protein (SBP) that binds Fe(III)
110 to deliver it to the Fut ABC transporter (21, 22). A functional homologue of FutA2 is the cytosolic
111 protein FutA1 that binds Fe(II) and protects the photosystem against oxidative stress (23-25);
112 however, FutA1 has also been shown to bind Fe(III) (21, 26). We have previously reported dual
113 localization and function for the single FutA protein of the marine cyanobacterium *Trichodesmium*
114 (27), suggesting it can bind both iron species. Similarly, *Prochlorococcus* harbors a single *futA*
115 gene (20), we wanted to understand whether and how a single FutA protein can bind both iron
116 species, and how redox plasticity was structurally encoded.

117 It is challenging to obtain crystallographic models without alteration of the metal sites, since site-
118 specific damage occurs extremely quickly and at very low doses (28), particularly for iron (29, 30).
119 Indeed, the FutA structure determined from a conventional diffraction experiment on an X-ray
120 home source reported here represented the photo-reduced, Fe(II) binding state, corroborated by
121 spectroscopic evidence. A serial femtosecond crystallography approach (SFX) using an XFEL
122 source and a complementary neutron diffraction approach were required to avoid the
123 manifestations of X-ray induced photoreduction in order to determine the Fe(III) state and give
124 protonation states of iron coordinating amino acid side chains. Using a fixed-target silicon chip
125 system for crystal delivery (31) at both synchrotron and XFEL radiation sources, we studied the
126 transition between Fe(III) to Fe(II) states whilst making use of the effects of X-ray induced
127 photoreduction, varying dose and time. The resulting protein structures support a dual binding
128 mode for iron and give insight into protein adaptation to evolutionary pressures.

129 Results

130 **The structure of FutA.** The crystallographic X-ray structure of FutA was determined from a
131 single crystal to 1.7 Å resolution, using a standard rotation protocol with the crystal in a sealed
132 capillary at a home source setup (**Table S1**). Substrate binding domains such as FutA can be
133 classified based on overall fold and *Prochlorococcus* FutA classifies as “D type” substrate binding
134 protein. The N-terminal (amino acids 1-98 and 232-280, light grey) and C-terminal domains
135 (amino acids 99-231 and 281-314, dark grey) are highlighted in **Fig. 1A**.

136 The substrate-binding cleft bears the iron-binding site that is open to the surrounding solvent. The
137 four tyrosine side chains of Tyr13 from N-terminal and Tyr143, Tyr199 and Tyr200 from C-
138 terminal domains coordinate the iron, **Fig. 1B**, in this Class IV substrate binding protein (32). The
139 trigonal bipyramidal coordination involves Tyr13, Tyr143 and Tyr200 to form the trigonal plane
140 with iron at its center, while Tyr199 and a coordinating solvent molecule are the axial ligands.

141 Interestingly, the structure reveals a positioning of two arginine side chains, Arg103 and Arg203,
142 in a second shell around the iron binding site, **Fig. 1C**. One might assume the tyrosine side
143 chains are negatively charged tyrosinates, and arginine side chains would each provide a positive
144 charge, with a neutral solvent molecule. To understand the charge state, we used spectroscopy
145 and confirmed protonation states using neutron diffraction.

146 **Determination of the Fe(III) iron binding state by spectroscopy.** A refolding protocol in
147 presence of iron sulfate was used to purify FutA. The burgundy red color of the purified protein
148 that can readily be bleached by excess sodium dithionite likely resulted from the ligand to metal
149 charge transfer (LMCT) bands between the tyrosinate residues coordinating the Fe(III) ion, **Fig.**
150 **2A.**

151 The electron paramagnetic resonance (EPR) spectrum of purified FutA shows a sharp signal at a
152 g-value of 4.29, **Fig. 2B**. This signal is indicative of a $|\pm 3/2\rangle$ doublet from a $3d^5$, high-spin ($S = 5/2$)

153 isotropic system ($E/D \approx 1/3$), consistent with an Fe(III) ion bound to FutA (33). The weaker signals
154 ($g = 5.67$, $g = 7.90$) derive from either $|\pm 1/2\rangle$ ground state transitions or from $|\pm 3/2\rangle$ resonances
155 from rhombic species of the Fe(III) iron. However, given the very high transition probabilities for
156 the $g = 4.29$ signal compared to the lower transition probability for ground state or anisotropic
157 species, the latter resonances likely represent a significant fraction of the total spins in the
158 sample. Excess of sodium dithionite leads to the loss of the EPR signal, **Fig. 2B**. This could result
159 from loss of iron binding and reduction in solution, or reduction of Fe(III) iron to a colorless and
160 $3d^6$ EPR-silent (probably $S=2$) Fe(II) state within the active site.

161 **Protonation state of Fe(III) coordinating residues as determined by neutron diffraction.** We
162 determined the crystallographic structure of FutA by neutron diffraction to 2.1 Å resolution
163 (**Tables S1 & S2**). Positive density in the neutron $F_o - F_c$ omit map indicates sites of successful
164 hydrogen-deuterium exchange. The lack of deuterium on the iron coordinating Tyr13, Tyr143,
165 Tyr199 and Tyr200 suggests these residues are tyrosinates, **Fig. 2C**. The nuclear density for the
166 metal-bound solvent is consistent with neutral water. Arg203 is not engaged in any interactions
167 and does not contribute to the second shell (**Fig. S1**), in contrast to the X-ray structure, **Fig. 1**.
168 However, side chain of Arg103 in the second shell is fully protonated and positively charged, thus
169 together with the four negatively charged tyrosinates Fe(III) binding results in an overall charge
170 balanced binding site.

171 **The Fe(III) iron state structure determined by serial femtosecond crystallography (SFX).**
172 The SFX experiment used short (10 fs), high-intensity X-ray pulses from the SACLX XFEL to
173 provide diffraction patterns that are collected before the crystal is destroyed (34). It has been
174 shown that data can be recorded free of the effects of radiation induced changes as long as
175 sufficiently short pulses (<20 fs) are used (35). Crystallization conditions were optimized to obtain
176 microcrystal slurries suitable for SFX, as described by us previously (36). For data collection,
177 crystals of approximately $20 \times 7 \times 7 \mu\text{m}^3$ were applied onto a fixed-target silicon chip, with the
178 final dataset merged from three chips (**Table S1**).

179 SFX and neutron diffraction structures are similar (see comparison in SI), with the Arg103 side
180 chain contributing to the second shell, but the side chain of Arg203 pointing away from the
181 binding site, **Fig. 2D**. EPR data, neutron diffraction and SFX agree and are consistent with iron
182 binding in the Fe(III) state. In turn, this suggests that the structure determined from the X-ray
183 home source with the Arg203 side chain pointing towards the binding site as shown in **Fig. 1** may
184 represent the Fe(II) state.

185 **Characterization of X-ray induced photoreduction of Fe(III) FutA.** The home source rotation
186 experiment might either fortuitously have captured the reduced state, or this observation had
187 resulted from X-ray induced photoreduction of Fe(III) to Fe(II). Photoreduction was highly likely,
188 considering the bleaching of the burgundy-red appearance in the X-ray exposed area of the
189 crystal during data collection. We thus went on to characterize the effect of X-ray exposure using
190 *in crystallo* optical spectroscopy (37).

191 The electronic absorption peak ($\lambda_{\text{max}} = 438 \text{ nm}$) corresponding to the Fe(III) iron (38)
192 progressively decays on incident X-ray irradiation at a synchrotron beamline, **Fig. 3A**. As X-rays
193 induce light-absorbing chemical species in the solvent that overlap with the Fe(III) iron specific
194 signal, the 620 nm wavelength was chosen to minimize the effect of this artefact and characterize
195 photoreduction of the iron center, plotting absorbance against accumulated radiation dose, **Fig.**
196 **3B**. Measuring five different crystals, we determined a half-photoreduction dose of $128 \pm 21 \text{ kGy}$;
197 the dose at which 80% of the molecules had been photoreduced was $204 \pm 27 \text{ kGy}$.

198 **Tracking of X-ray induced photoreduction from an SSX dose series.** A fixed target serial
199 synchrotron crystallography (SSX) approach described by us previously (31) was used, as it is
200 well suited for low dose investigations. A series of ten images was taken from each microcrystal,

201 where each image incrementally increases the dose, allowing us to follow structural changes of
202 the FutA iron complex in response to X-ray induced photoreduction.

203 Two different dose series with dose increments of 5 kGy and 22 kGy are reported (**Tables S3 &**
204 **S4**). Images corresponding to each dose point are merged to provide a series of datasets
205 corresponding to these dose points. The isomorphous difference density indicates an alternative
206 conformation for Arg203. The feature is readily visible at 22 kGy and strongest at 88 kGy, **Fig.**
207 **3C**. Indeed, overlay with the conformation observed in the home source structure, **Fig. 1C**, shows
208 that both structures are similar, suggesting the photoreduced state was observed in either case.

209 **An XFEL X-ray pump-probe (XRPP) approach captures the transition between Fe(III) and**
210 **Fe(II) states.** We designed a novel serial femtosecond crystallography experiment where a first
211 pulse, attenuated using a sapphire wafer mounted on a fast flipper, was followed by a second,
212 unattenuated pulse (**Fig. S2**). Using SACLA's repetition rate of 30 Hz, the 10 fs pump and probe
213 were spaced 33 ms apart. While several different levels of attenuation were explored, data for a
214 350 kGy pump (94% attenuated) yielded structural changes consistent with photoreduction.
215 Interestingly, in contrast to the SSX series, **Fig. 3C**, this experiment preserved the iron
216 coordinating water that was clearly resolved in electron density, **Fig. 4**, consistent with penta-
217 coordinated Fe(II) iron. Ensuing refinement confirms presence of the alternative conformation of
218 Arg203 (**Fig. S3**). For the high occupancy state of Arg203 with the guanidino group closest to the
219 iron center, distances were 4.8 Å between the η 1 amide of Arg203 and the phenolate oxygen of
220 Tyr200, and 4.6 Å between the η 2 amide of Arg203 and the alkoxy group of Tyr13. The XRPP
221 experiment thus induced specific alteration(s) and created the FutA Fe(II) state *in situ*.

222 **Discussion**

223 The adaptation of the marine cyanobacterium *Prochlorococcus* is a remarkable story of ecological
224 success, making this photosynthetic organism the most abundant on earth. Two factors are
225 particularly important, the ability to survive under limiting nutrient conditions and physical size
226 reduction where both factors put evolutionary pressure on the iron uptake system of the
227 bacterium (13, 14). This study addresses the challenge of how a single gene product, FutA, can
228 bind both Fe(III) and Fe(II) iron.

229 The structural analyses reported at ambient (room) temperature allow delineating a plausible
230 mechanism for iron binding in two different oxidation states, showing how FutA Arg203 operates
231 as a switch between states. The side chain of this residue is not engaged in polar contacts in the
232 Fe(III) states, which is hinting at its intrinsic dynamics, allowing it to be recruited and engage in
233 interaction with the iron center and contribute a balancing charge in the Fe(II) state, **Fig. 3D**.

234 X-ray crystallographic study of RedOx active metallo-proteins is challenging as X-ray induced
235 photoreduction can occur. Transition metals are particularly sensitive to specific radiation damage
236 (28, 39), and observation of the FutA Fe(III) state required SFX / neutron diffraction. Changes in
237 the oxidation state induced by X-rays were previously documented for doses as low as 30 - 20
238 kGy (30, 40, 41). For Fe(III), we show that the half-point for photoreduction in FutA corresponds
239 to a dose of 128 +/- 21 kGy, as shown by spectroscopic analysis, **Fig. 2B**.

240 We exploited the effects of X-ray induced photoreduction to study the transition between Fe(III)
241 and Fe(II) states, using a SSX dose series and an SFX X-ray pump probe setup, both allowing us
242 to map conformational changes at ambient temperatures (42). The major difference observed
243 between these approaches occurred for density of the coordinating water, which disappeared
244 with accumulating dose in SSX, **Fig. 3C**, while the SFX XRPP approach preserved the electron
245 density, **Fig. 4**. The reported doses delivered were 350 kGy in a 10-femtosecond pulse in the
246 SFX XRPP pump which was 3.2 and 4 times higher than the doses used in the home source and
247 SSX experiments, respectively, both of which used continuous X-ray exposure which could lead
248 to difference in heat load. Beam sizes were also different, with 300 micron for home source, 10

249 micron for SSX and 1.5 micron for SFX experiments, providing an important difference for photo-
250 electron escape (43). Further work is needed to understand radiation chemistry arising from these
251 different conditions (see additional discussion in SI).

252 Discovery of a mechanism to bind two different iron oxidation states prompted us to revisit
253 homologues of the *FutA* iron binding protein, and we found that a similar switch may exist for the
254 iron binding protein *FbpA* from *Thermus thermophilus* with structures in two states reported (**Fig.**
255 **S4**). *Synechocystis* has two specialized iron binding proteins, with *FutA2* being assigned a Fe(III)
256 binding function in the oxidative environment of the periplasm, while *FutA1* binds Fe(II) iron
257 favored under reducing conditions in the cytosol. For these proteins, conservation of the arginine
258 residue equivalent *Prochlorococcus* Arg203 (**Fig. S5**) may relate to biological ability to bind iron at
259 different oxidation states, as discussed in supplementary text.

260 **Conclusion:** Structures with iron bound in different oxidation states help explain how the intrinsic
261 structural plasticity of *FutA* accommodate Fe(II) as well as Fe(III) iron species. Translated into a
262 molecular mechanism, an arginine side chain flip provides a charge balance. The acute sensitivity
263 of *FutA* to specific radiation damage illustrates the requirement for dose limiting data collection
264 regimes. We have used photoreduction as an advantage to study the transition of Fe(III) to Fe(II)
265 binding state. The X-ray pump probe approach demonstrated here has the potential to become a
266 straightforward-to-implement approach to induce redox state changes probing structural
267 transitions. We envisage that more complex experiments could generate photoreduced states
268 akin to anaerobic conditions that are amenable for further modification by ligand addition.

269 Materials and Methods

270 The sections *molecular biology; protein purification; protein crystallization; sample preparation for*
271 *serial crystallography; crystallographic data processing; structure determination and refinement;*
272 *in crystallo UV-vis spectroscopy* are found in SI. All studies (except EPR) were performed at
273 ambient (room) temperature. Crystallization used the natural pH of the purification buffer (0.1 M
274 Tris buffered at pH 9.0, containing 320 mM NaCl), and 12% (w/v) PEG3350 / 0.2 M NaSCN in
275 vapor diffusion for the home source and in batch for neutron diffraction structures. Seeded batch
276 crystallization with 20% (w/v) PEG3350 / 0.2 M NaSCN was used for serial crystallography.
277 Diffraction-weighted doses (DWD) reported include photoelectron escape calculation with
278 *RADDose-3D* (version 2.1) (44) (for a critical discussion on dose calculation see SI).

279 *Home source crystal structure.* Data were collected from a single crystal grown from batch
280 crystallization and measuring $0.23 \times 0.24 \times 0.12 \text{ mm}^3$, mounted in a 0.7 mm sealed quartz
281 capillary on a Rigaku 007 HF (High Flux) diffractometer equipped with a HyPix 6000HE detector.
282 The X-ray beam with a flux of $2.5 \times 10^9 \text{ ph/s}$ at 8.1 keV was collimated at $200 \mu\text{m}^2$. The total
283 exposure time of 1 hr equated to a total dose of 110 kGy.

284 *Neutron crystallography.* For hydrogen-deuterium exchange, Fe(III) loaded *FutA* crystals grown
285 from batch crystallization were transferred into a deuterated solution of the same crystallization
286 conditions, in two subsequent exchanges for 24 hrs. Crystals with a volume larger than 0.2 mm^3
287 were mounted in 1 mm sealed quartz capillaries. Data collection at BIODIFF (45),
288 Forschungsreaktor München II (Germany) used a monochromatic neutron beam. The final
289 dataset was merged from two isomorphous crystals collected at wavelengths of 3.1 \AA (calibrated
290 to 4DP with an Yttrium Iron Garnet powder sample).

291 *Serial synchrotron crystallography (SSX).* SSX data were collected at beamline I24, Diamond
292 Light Source, using silicon chips with $12 \mu\text{m}$ apertures. For each dose series, ten images (10 ms
293 per image) were collected at each aperture. Images were separated into individual dose points for
294 processing to obtain ten dose points (40). Datasets above a total dose of 110 kGy were no longer
295 isomorphous with the lowest dose point, with increased B-factors corroborating global damage.

296 *Serial femtosecond crystallography (SFX)*. SFX data were collected at SACLÀ beamline BL2
297 EH3, Japan, using the MPCCD detector. The XFEL was operated at an X-ray energy of 11.0 keV
298 with a pulse length of 10 fs and a repetition rate of 30 Hz. Synchronizing chip translation with the
299 XFEL pulse, data collection took roughly 14 mins per chip.

300 *SFX X-ray pump probe*. For the XRPP experiments, a flipper-attenuator was used to reduce the
301 flux of alternate XFEL pulses. A fast, self-restoring rotary shutter (Branstrom Instruments, USA)
302 mounted upstream of the sample and containing Sapphire wafer in a range of thicknesses was
303 triggered, via TTL from a signal generator, to move the wafer into and out of the X ray beam path.
304 Pump and probe diffraction images were separated based on total scattering intensity using the
305 dxtbx.radial_average function from the DIALS software package (**Fig. S2**).

306 *UV-vis absorption spectroscopy*. In solution spectra were collected in purification buffer (0.1 M
307 Tris buffered at pH 9.0, containing 320 mM NaCl) on a Shimadzu UV-2600 spectrophotometer at
308 a protein concentration of 4.75 mg/ml (0.14 mM). In the chemical reaction experiment, Na₂S₂O₄
309 was added to a final concentration of 1.4 mM under aerobic conditions. *In crystallo* X-ray dose
310 dependent UV-vis absorption spectroscopy was performed at ESRF beamline BM07-FIP2 with a
311 200 x 200 μm^2 X-ray top-hat beam at 12.66 keV (4.1 and 5.0 x 10¹¹ ph/s photon flux). Spectra
312 were acquired at 0.4 Hz with a loop-mount crystal using a humidity controller (HC-Lab, Arinax)
313 (46) bathed in the X-ray beam on an online microspectrophotometer with a focal volume of 50 x
314 50 x ~100 μm^3 (37, 47).

315 *Electron paramagnetic resonance*. FutA at a concentration of 50 μM was shock-frozen in liquid
316 nitrogen. In the chemical reduction experiment, Na₂S₂O₄ was added to a final concentration of
317 500 μM under aerobic conditions prior to freezing. Data collection was carried out in EPR quartz
318 tubes at liquid helium temperature. X-band continuous wave EPR spectra (10 Gauss modulation
319 amplitude, 2 mW microwave power) were recorded on a Bruker eleXsys E500 spectrometer using
320 a standard rectangular Bruker EPR cavity (ER4102T) equipped with an Oxford helium cryostat
321 (ESR900) at 5 – 6 K.

322 Acknowledgments

323 We thank Chris Holes for macromolecular crystallization, Peter Horton for diffraction, and Peter
324 Roach for critical discussion at the University of Southampton (UoS). Financial support: Japan
325 Partnering Award, Biological Sciences Research Council (BBSRC) BB/R021015/1,
326 BB/W001950/1 to JW, MH, RO; Diamond Doctoral Studentship Programme to RB, JS, MR, CC;
327 South Coast Biosciences Doctoral Training Partnership SoCoBio DTP BBSRC BB/T008768/1 to
328 JS; PhD studentships by Hamburg University and the European Synchrotron Radiation Facility
329 (ESRF) to NC, the Collaborative Computing Project 4 (CCP4) to LC (#7920S22020007); the
330 Institute for Life Sciences (Southampton) to CC; Wellcome Investigator Award 210734/Z/18/Z to
331 AMO; Royal Society Wolfson Fellowship RSWF\R2\182017 to AMO. We acknowledge facility
332 access to the National Crystallography Service (NCS) Southampton; DLS MX15722, NT14493,
333 NT23570; SACLÀ 2022A8002, 2022B8041; Forschungsreaktor München ID:16106; ESRF BM07-
334 FIP2 and *i*COS, MX2373, MX2374; Diamond Light Source (DLS) UK XFEL hub and ESRF for
335 travel support. We are grateful to beamline staff, in particular Shigeki Owada and Kensuke Tono
336 at SACLÀ.

337 References

- 338 1. K. Hans Wedepohl, The composition of the continental crust. *Geochimica et
339 Cosmochimica Acta* **59**, 1217-1232 (1995).
- 340 2. P. W. Boyd *et al.*, Mesoscale Iron Enrichment Experiments 1993-2005: Synthesis and
341 Future Directions. *Science* **315**, 612-617 (2007).

342 3. W. Stumm, B. Sulzberger, The cycling of iron in natural environments: Considerations
343 based on laboratory studies of heterogeneous redox processes. *Geochimica et*
344 *Cosmochimica Acta* **56**, 3233-3257 (1992).

345 4. M. L. Wells, N. M. Price, K. W. Bruland, Iron chemistry in seawater and its relationship to
346 phytoplankton: a workshop report. *Marine Chemistry* **48**, 157-182 (1995).

347 5. H. W. Rich, F. M. M. Morel, Availability of well-defined iron colloids to the marine diatom
348 *Thalassiosira weissflogii*. *Limnology and Oceanography* **35**, 652-662 (1990).

349 6. J. A. Raven, M. C. W. Evans, R. E. Korb, The role of trace metals in photosynthetic
350 electron transport in O₂-evolving organisms. *Photosynthesis Research* **60**, 111-150
351 (1999).

352 7. S. Richier *et al.*, Abundances of Iron-Binding Photosynthetic and Nitrogen-Fixing Proteins
353 of *Trichodesmium* Both in Culture and In Situ from the North Atlantic. *PLoS ONE* **7**,
354 e35571 (2012).

355 8. J. T. Snow *et al.*, Quantifying Integrated Proteomic Responses to Iron Stress in the
356 Globally Important Marine Diazotroph *Trichodesmium*. *PLOS ONE* **10**, e0142626 (2015).

357 9. Z. S. Kolber *et al.*, Iron limitation of phytoplankton photosynthesis in the equatorial Pacific
358 Ocean. *Nature* **371**, 145-149 (1994).

359 10. M. C. Moore *et al.*, Large-scale distribution of Atlantic nitrogen fixation controlled by iron
360 availability. *Nature Geoscience* **2**, 867-871 (2009).

361 11. M. A. Huston, S. Wolverton, The global distribution of net primary production: resolving
362 the paradox. *Ecological Monographs* **79**, 343-377 (2009).

363 12. P. Flombaum *et al.*, Present and future global distributions of the marine cyanobacteria
364 *Prochlorococcus* and *Synechococcus*. *Proceedings of the National Academy of Sciences*
365 **110**, 9824-9829 (2013).

366 13. S. J. Biller, P. M. Berube, D. Lindell, S. W. Chisholm, *Prochlorococcus*: the structure and
367 function of collective diversity. *Nature Reviews Microbiology* **13**, 13-27 (2015).

368 14. F. Partensky, W. R. Hess, D. Vaulot, *Prochlorococcus*, a Marine Photosynthetic
369 Prokaryote of Global Significance. *Microbiology and Molecular Biology Reviews* **63**, 106-
370 127 (1999).

371 15. P. M. Berube *et al.*, Single cell genomes of *Prochlorococcus*, *Synechococcus*, and
372 sympatric microbes from diverse marine environments. *Sci Data* **5**, 180154 (2018).

373 16. R. Sutak, J.-M. Camadro, E. Lesuisse, Iron Uptake Mechanisms in Marine Phytoplankton.
374 *Frontiers in Microbiology* **11** (2020).

375 17. M. Sandy, A. Butler, Microbial Iron Acquisition: Marine and Terrestrial Siderophores.
376 *Chemical Reviews* **109**, 4580-4595 (2009).

377 18. D. B. Rusch, A. C. Martiny, C. L. Dupont, A. L. Halpern, J. C. Venter, Characterization of
378 *Prochlorococcus* clades from iron-depleted oceanic regions. *Proceedings of the National
379 Academy of Sciences* **107**, 16184-16189 (2010).

380 19. R. R. Malmstrom *et al.*, Ecology of uncultured *Prochlorococcus* clades revealed through
381 single-cell genomics and biogeographic analysis. *International Society for Microbial
382 Ecology Journal* **7**, 184-198 (2013).

383 20. G. Rocap *et al.*, Genome divergence in two *Prochlorococcus* ecotypes reflects oceanic
384 niche differentiation. *Nature* **424**, 1042-1047 (2003).

385 21. H. Katoh, N. Hagino, A. R. Grossman, T. Ogawa, Genes essential to iron transport in the
386 cyanobacterium *Synechocystis* sp. strain PCC 6803. *Journal of Bacteriology* **183**, 2779-
387 2784 (2001).

388 22. A. Badarau *et al.*, *FutA2* is a ferric binding protein from *Synechocystis* PCC 6803. *Journal
389 of Biological Chemistry* **283**, 12520-12527 (2007).

390 23. P. Exss-Sonne, J. Tölle, K. P. Bader, E. K. Pistorius, K.-P. Michel, The *IdiA* protein of
391 *Synechococcus* sp. PCC 7942 functions in protecting the acceptor side of Photosystem II
392 under oxidative stress. *Photosynthesis Research* **63**, 145-157 (2000).

393 24. J. Tölle *et al.*, Localization and function of the *IdiA* homologue *Slr1295* in the
394 cyanobacterium *Synechocystis* sp. strain PCC 6803. *Microbiology* **148**, 3293-3305
395 (2002).

396 25. K. P. Michel, E. K. Pistorius, Adaptation of the photosynthetic electron transport chain in
397 cyanobacteria to iron deficiency: The function of IdiA and IsiA. *Physiologia Plantarum*
398 **120**, 36-50 (2004).

399 26. H. Katoh, N. Hagino, T. Ogawa, Iron-binding activity of FutA1 subunit of an ABC-type iron
400 transporter in the cyanobacterium Synechocystis sp. Strain PCC 6803. *Plant and Cell
401 Physiology* **42**, 823-827 (2001).

402 27. D. Polyviou *et al.*, Structural and functional characterization of IdiA/FutA (Tery_3377), an
403 iron-binding protein from the ocean diazotroph *Trichodesmium erythraeum*. *Journal of
404 Biological Chemistry* **293**, 18099-18109 (2018).

405 28. E. F. Garman, M. Weik, Radiation Damage in Macromolecular Crystallography. *Methods
406 Mol Biol* **1607**, 467-489 (2017).

407 29. J. A. R. Worrall, M. A. Hough, Serial femtosecond crystallography approaches to
408 understanding catalysis in iron enzymes. *Curr Opin Struc Biol* **77** (2022).

409 30. V. Pfanzagl *et al.*, X-ray-induced photoreduction of heme metal centers rapidly induces
410 active-site perturbations in a protein-independent manner. *Journal of Biological
411 Chemistry* **295**, 13488-13501 (2020).

412 31. S. Horrell *et al.*, Fixed Target Serial Data Collection at Diamond Light Source. *J Vis Exp*
413 10.3791/62200 (2021).

414 32. S. Wang *et al.*, A novel mode of ferric ion coordination by the periplasmic ferric ion-
415 binding subunit FbpA of an ABC-type iron transporter from *Thermus thermophilus* HB8.
416 *Acta Crystallographica Section D* **70**, 196-202 (2014).

417 33. G. Palmer, The electron paramagnetic resonance of metalloproteins. *Biochem Soc Trans*
418 **13**, 548-560 (1985).

419 34. H. N. Chapman, X-Ray Free-Electron Lasers for the Structure and Dynamics of
420 Macromolecules. *Annu Rev Biochem* **88**, 35-58 (2019).

421 35. K. Nass *et al.*, Structural dynamics in proteins induced by and probed with X-ray free-
422 electron laser pulses. *Nat Commun* **11**, 1814 (2020).

423 36. J. H. Beale *et al.*, Successful sample preparation for serial crystallography experiments.
424 *Journal of Applied Crystallography* **52**, 1385-1396 (2019).

425 37. D. von Stetten *et al.*, In crystallo optical spectroscopy (icOS) as a complementary tool on
426 the macromolecular crystallography beamlines of the ESRF. *Acta Crystallogr D Biol
427 Crystallogr* **71**, 15-26 (2015).

428 38. A. M. Orville, N. Elango, J. D. Lipscomb, D. H. Ohlendorf, Structures of competitive
429 inhibitor complexes of protocatechuate 3,4-dioxygenase: multiple exogenous ligand
430 binding orientations within the active site. *Biochemistry* **36**, 10039-10051 (1997).

431 39. M. A. Hough, R. L. Owen, Serial synchrotron and XFEL crystallography for studies of
432 metalloprotein catalysis. *Curr Opin Struct Biol* **71**, 232-238 (2021).

433 40. A. Ebrahim *et al.*, Dose-resolved serial synchrotron and XFEL structures of radiation-
434 sensitive metalloproteins. *International Union of Crystallography Journal* **6**, 543-551
435 (2019).

436 41. I. G. Denisov, D. C. Victoria, S. G. Sligar, Cryoradiolytic reduction of heme proteins:
437 Maximizing dose-dependent yield. *Radiation Physics and Chemistry* **76**, 714-721 (2007).

438 42. J. S. Fraser *et al.*, Accessing protein conformational ensembles using room-temperature
439 X-ray crystallography. *Proc Natl Acad Sci U S A* **108**, 16247-16252 (2011).

440 43. S. L. S. Storm *et al.*, Measuring energy-dependent photoelectron escape in microcrystals.
441 *IUCrJ* **7**, 129-135 (2020).

442 44. C. S. Bury, J. C. Brooks-Bartlett, S. P. Walsh, E. F. Garman, Estimate your dose:
443 RADDOS-3D. *Protein Science* **27**, 217-228 (2018).

444 45. T. S. A. Ostermann, BIODIFF: Diffractometer for large unit cells. *Journal of large-scale
445 research facilities* **1**, A2 (2015).

446 46. J. Sanchez-Weatherby *et al.*, Improving diffraction by humidity control: a novel device
447 compatible with X-ray beamlines. *Acta Crystallogr D Biol Crystallogr* **65**, 1237-1246
448 (2009).

449 47. J. McGeehan *et al.*, Colouring cryo-cooled crystals: online microspectrophotometry. *J*
450 *Synchrotron Radiat* **16**, 163-172 (2009).

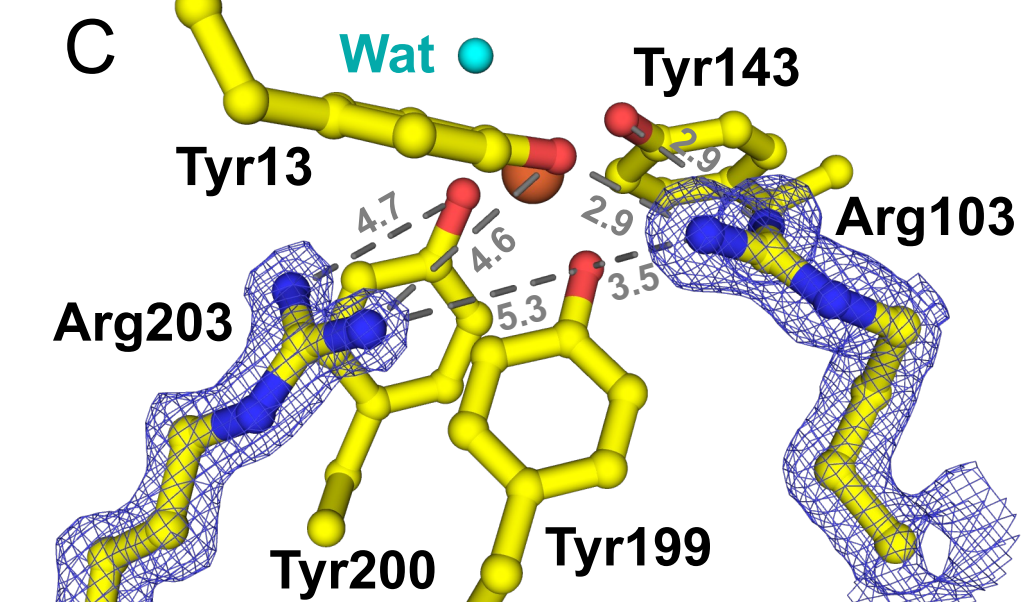
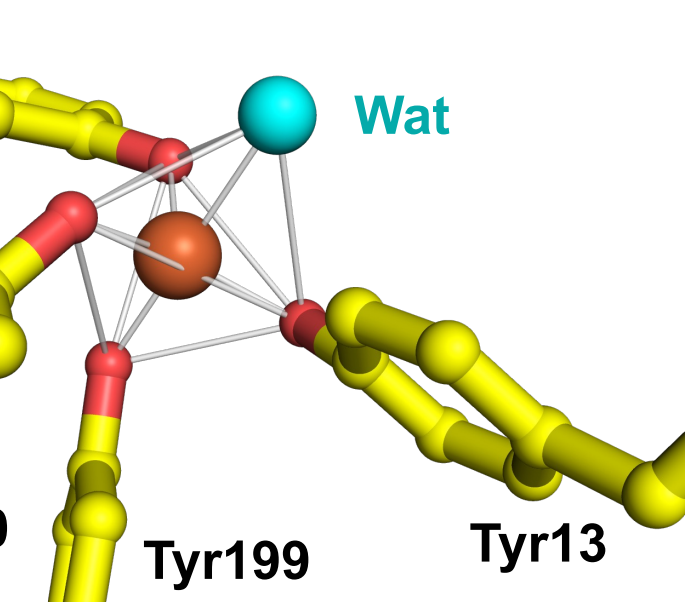
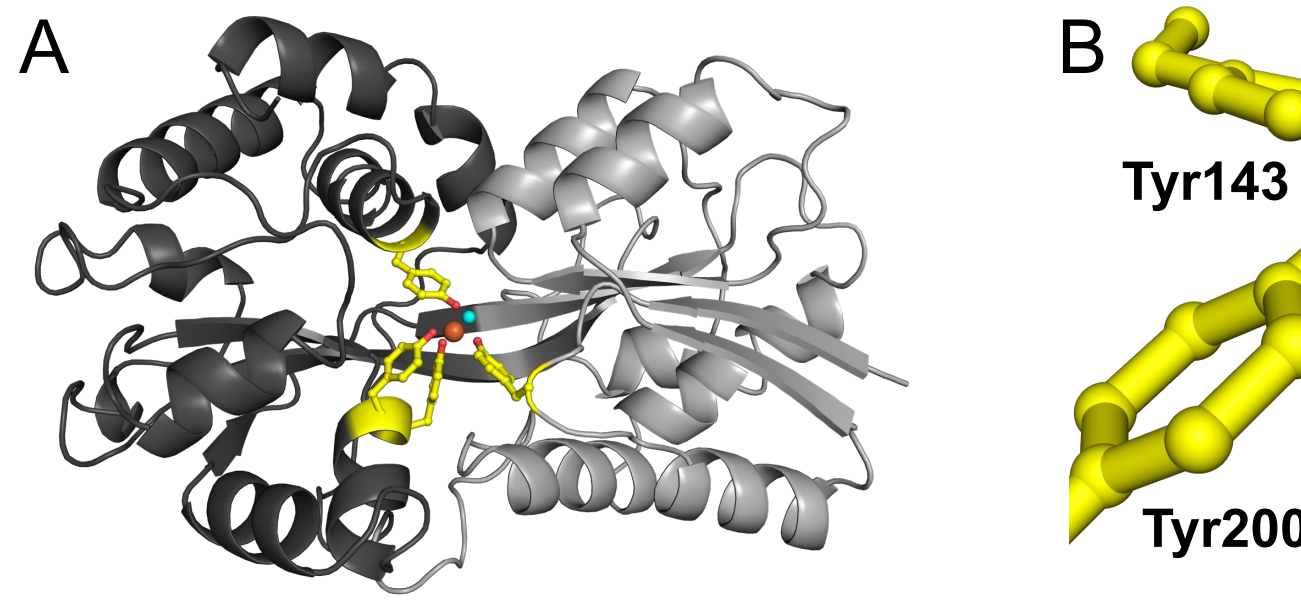
451 **Figures and Tables**

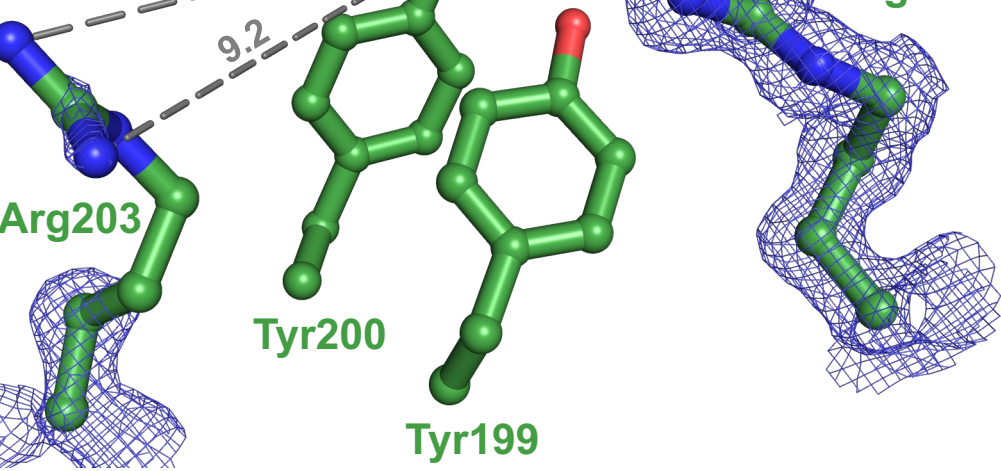
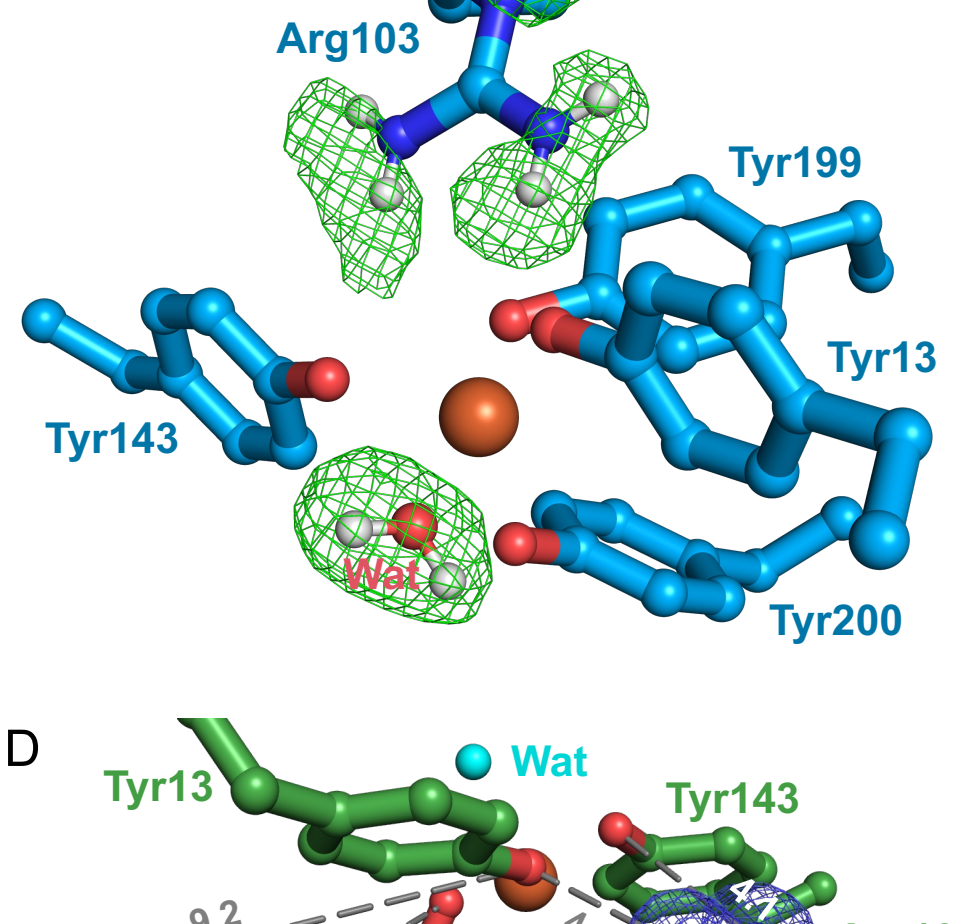
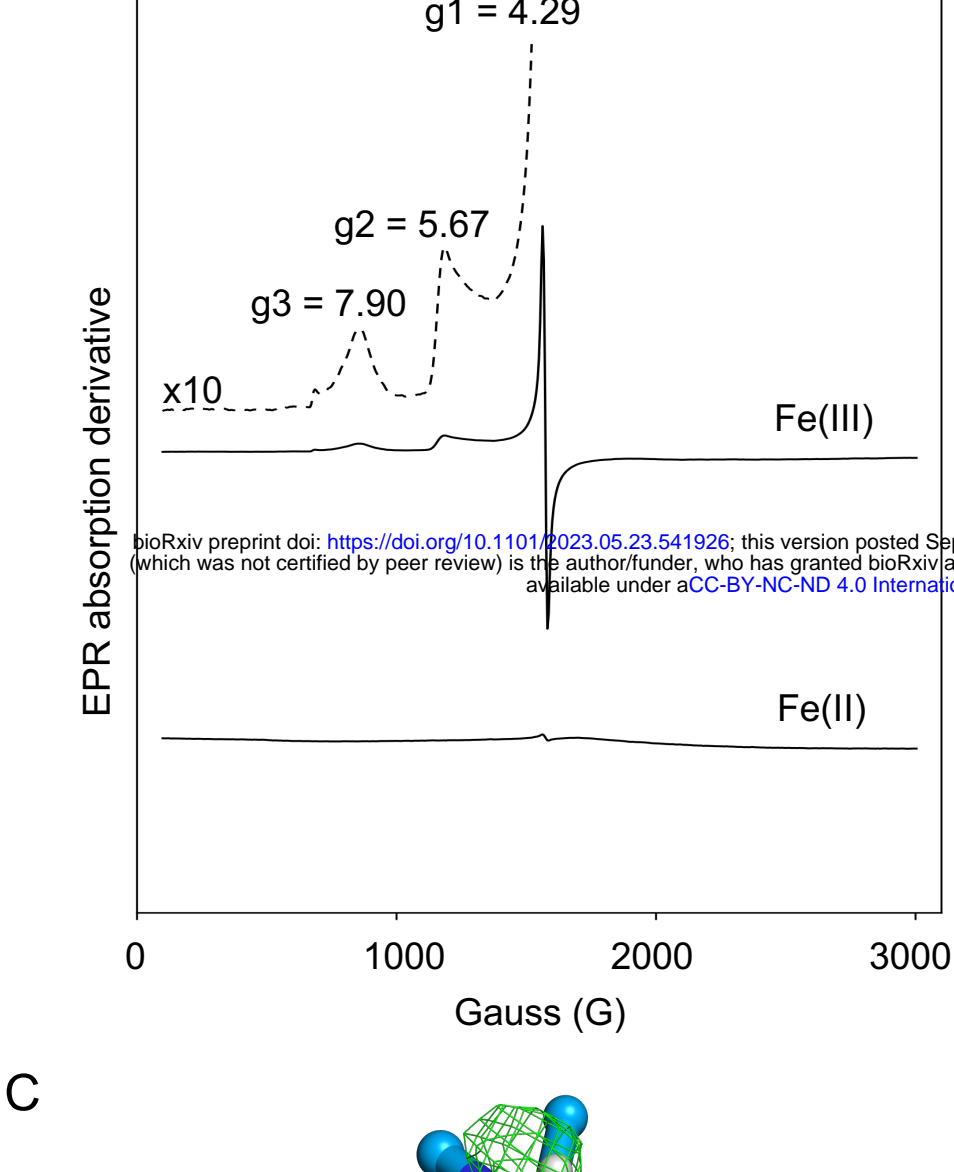
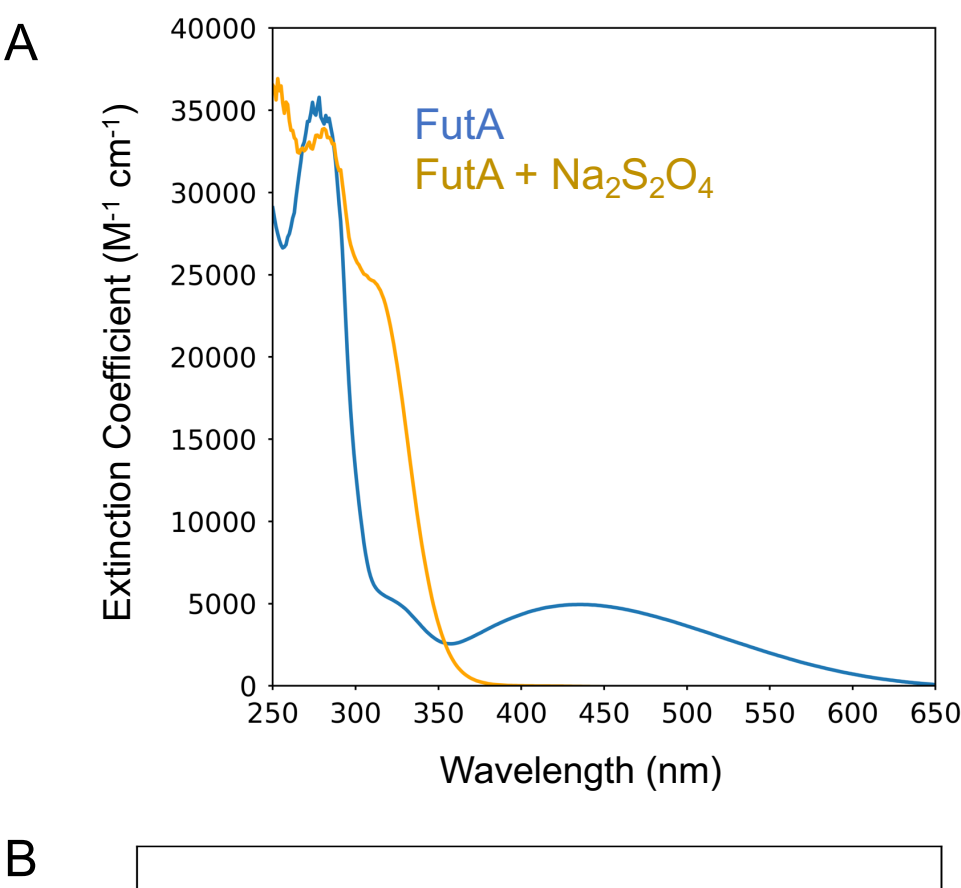
452 **Figure 1.** The Fe(II) state FutA structure from an X-ray home source determined to 1.7 Å
453 resolution. (A) FutA has a bi-lobal structure with the substrate binding cleft between the N-
454 terminal (light grey) and C-terminal domains (dark grey). Amino acid side chains contributing to
455 iron binding are shown in stick representation (yellow). (B) Trigonal bipyramidal coordination of
456 the iron, with Tyr199 and a solvent molecule as axial ligands. (C) The two arginine side chains of
457 Arg103 and Arg203 are in a second coordination shell, shown here with refined density ($2F_{\text{obs}} -$
458 F_{calc} , blue map, contoured at 1.5 σ). Color coding is yellow for carbon, red for oxygen, blue for
459 nitrogen, orange for iron, with the solvent molecule in light blue.

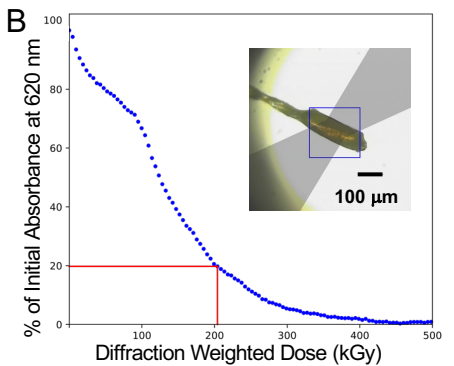
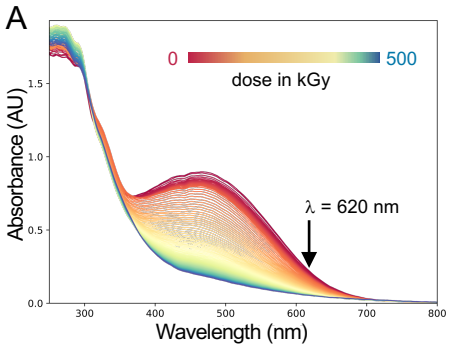
460 **Figure 2.** The FutA Fe(III) state characterized by UV-vis and EPR spectroscopy, neutron
461 diffraction and serial femtosecond crystallography. (A) The UV-vis spectrum of recombinantly
462 produced and purified FutA (blue) shows an absorbance maximum at 438 nm, consistent with
463 Fe(III) bound to FutA. The peak at 438 nm disappears after addition of 10-fold molar excess
464 sodium dithionite; the absorbance maximum at 315 nm indicates free sodium dithionite (yellow).
465 (B) EPR spectrum of purified and sodium dithionite reduced FutA. The peaks observed were: g_1
466 = 4.29 g, g_2 = 5.67 g, g_3 = 7.9 g. (C) The positive nuclear density in the neutron diffraction crystal
467 structure (green mesh, $F_{\text{obs}} - F_{\text{calc}}$ omit map at 3 σ , 2.1 Å resolution) indicates sites that have
468 undergone hydrogen-deuterium exchange, showing an oriented water as axial ligand (refined
469 deuterium fraction > 0.80). Arg103 fully protonated and positively charged, while the four tyrosine
470 side chains do not show difference density, suggesting they are negatively charged tyrosinates.
471 (D) The SFX crystal structure shows that the side chain of Arg203 is not oriented towards the
472 binding site and does not engage in polar interactions (similar to the neutron diffraction structure
473 **Fig. S1**). Carbons shown blue (neutron diffraction) or green (SFX), heteroatoms colored as in
474 **Fig. 1**.

475 **Figure 3.** X-ray induced photoreduction of FutA characterized by spectroscopy and SSX. (A)
476 Successive UV-vis absorption spectra collected *in crystallo* plotted for a FutA crystal during X-ray
477 exposure, from 0 kGy (red) to 500 kGy (blue). Photoreduction was monitored at a wavelength of
478 620 nm (arrow). (B) Evolution of the normalized absorbance at 620 nm, collected on a single
479 crystal. In the example shown, 80% of the signal was lost at 204 ± 27 kGy (red lines). Inset:
480 geometry of the experiment. The light path for the spectroscopic measurement is indicated in
481 grey. (C) SSX dose series at RT. Top: refined structure at 5 kGy (carbon atoms shown in purple;
482 $2F_{\text{O}} - F_{\text{C}}$ density in blue contoured at 1.5 σ , $F_{\text{O}} - F_{\text{C}}$ in green contoured at 3 σ). Pronounced
483 difference density is seen at 22 kGy and 88 kGy, suggesting Arg203 takes an alternative
484 conformation, as indicated by overlay with the conformation seen in the Fe(II) state determined
485 from the home source (Arg203 carbons shown in yellow for the 88 kGy dose point). Heteroatoms
486 colored as in **Fig. 1**. (D) Charges of amino acids contributing to the coordination sphere and
487 second shell for the Fe(III) and Fe(II) binding states, assuming an overall neutral state of the
488 binding site.

489 **Figure 4.** SFX X-ray pump probe experiment. The model of the Fe(III) iron state determined SFX
490 (compare **Fig. 2D**) was used in refinement against an SFX probe dataset, collected after a 350
491 kGy pump. Refined electron density shows Tyr13 in a double conformation, but limited density for
492 the Arg203 guanidino group ($2F_{\text{O}} - F_{\text{C}}$, blue, 1.5 σ); however, difference density ($F_{\text{O}} - F_{\text{C}}$, green, 3 σ)
493 suggests that Arg203 takes an alternative conformation similar to the conformation observed in
494 the Fe(II) state determined from the home source (Arg203 carbons shown in yellow).
495 Heteroatoms colored as in **Fig. 1**.







D

coordination sphere					second shell			Fe
Tyr13	Tyr143	Tyr199	Tyr200	Wat	Arg103	Arg203	too far	+3
-1	-1	-1	-1	0	+1	+1	+2	Ferric
-1	-1	-1	-1	0	+1	+1	+2	Ferrous

